Network Synchronization and Synchrony Propagation: Emergent Elements of Inspiration

Authors: Sufyan Ashhad and Jack L Feldman*

Affiliation: Department of Neurobiology
Box 951763
University of California Los Angeles
Los Angeles, CA 90095-1763 USA

*Corresponding author: feldman@g.ucla.edu

ABSTRACT

While now well established that the preBötzinger Complex (preBötC)[1] is the kernel of breathing rhythmogenesis in mammals, the underlying mechanisms remain a mystery[2]. Critically, two long-favored hypotheses for rhythmogenesis, i.e., that the rhythm is generated by pacemaker neurons or by simple circuits dependent on inhibition including post-inhibitory rebound, are not supported by experimental tests[2-8]. Here, we explore an alternative (though non-exclusive) hypothesis, that the rhythm is an emergent property of the preBötC microcircuit[2,6,9,10]. We assessed preBötC network dynamics by recording synaptic inputs to preBötC neurons under respiratory rhythmic and non-rhythmic conditions in *in vitro* slices from neonatal mouse. Our analyses uncover a dynamic reorganization of preBötC network activity correlated with and, we hypothesize, essential to, rhythmicity. In each cycle under rhythmic conditions, an inspiratory burst (I-burst) emerges as (presumptive) preBötC rhythmogenic neurons transition away from aperiodic uncorrelated population spike activity to become increasingly synchronized during preinspiration; this burst activity subsides and the cycle repeats. Strikingly, in a slice in non-rhythmic conditions, antagonizing $GABA_A$ receptors can initiate this periodic synchronization and consequent rhythm, while simultaneously inducing a higher conductance (HC) state in preBötC nonrhythmogenic output neurons. This co-emergence of input synchrony and HC state in these output neurons unveils a novel network mechanism for generation of the rhythm that emerges in preBötC and that ultimately propagates to inspiratory motoneurons, effecting inspiratory muscle contraction and consequential breathing movements. In the light of divergent projections of preBötC output neurons through mono- and oligo-synaptic connections[11], synchronized oscillations in inspiratory motoneurons[12,13] and entrainment of limbic neurons by respiratory corollary discharge[14], we hypothesize that the evolution and propagation of preBötC synchrony plays a critical role in the extraordinary reliability and robustness of networks underlying respiratory motor output as well as in the use of breathing rhythms for binding of activity with and across higher brain regions.

MAIN TEXT

Brainstem slices from neonatal rodents containing the preBötC bathed in artificial cerebrospinal fluid (ACSF) with normal brain K^+ (3 mM) and Ca^{2+} (1.5 mM) concentrations are nonrhythmic[1] (Figs. 1a1, S1a1). However, with elevated $[K^+]_{ACSF}$ (9 mM), rhythmic I-bursts emerge in preBötC that in almost all instances cause motor-related I-bursts in hypoglossal nerve (XIIn; Figs. 1a2, a3, S1a2, a3). In each cycle, for up to a few hundred milliseconds prior to the rapid onset of I-bursts,

preBötC population activity grows slowly. This epoch is designated preinspiration (preI) and has a duration of ~250 msec *in vitro* (Fig. 1a4). Notably, when preI fails to induce a preBötC I-burst, the result is a low amplitude preBötC burstlet with no associated XIIn I-burst[9].

We explored the network dynamics underlying the generation and propagation of I-bursts by recording synaptic inputs impinging upon preBötC somatostatin-expressing (SST^+) neurons. These glutamatergic preBötC output neurons project to inspiratory premotor neurons[11,15-17] and are necessary for breathing *in vivo*[18]. Under non-rhythmic conditions where preBötC population bursts were absent or sporadic (3 mM $[K^+]_{ACSF}$; Fig 1a1, b1), preBötC SST^+ neurons received temporally dispersed asynchronous synaptic inputs that rarely summated to produce action potentials (APs; Fig. 1b1, c1)). However, with further depolarization induced by increasing $[K^+]_{ACSF}$ to 9 mM, their excitatory postsynaptic potentials (EPSPs) became periodic and clustered, producing more action potentials (APs) at shorter intervals prior to the I-burst; this increased activity percolated and grew, ultimately resulting in I-bursts (Figs. 1b2, b3; S1b1-b2). Using wavelet analysis to ascertain the EPSP spectrotemporal structure, we found that the membrane potential (V_m) power in the frequency range 4-64 Hz of I-modulated (I-M) preBötC SST^+ neurons (15/29) significantly increased during preI and subsequent I-bursts (Fig. 1c1-c2). During this period, synchronization of EPSPs progressively increased, with inputs at lower frequencies appearing first during preI (Figs. 1c3, 2f). Two notable points: i) preBötC I-M SST^+ neurons rarely fired APs during preI (Fig. S1b1-b2; similar to inspiratory Type-2 neurons[19]) making them an unlikely source for preI activity, and; ii) the frequency of synaptic inputs in the interburst intervals (IBIs) preceding preI decreased as compared to that during nonrhythmic conditions where low frequency inputs (4Hz–8 Hz) were only sporadically present (Fig. 1c1).

What kind of network interactions result in the emergence of synchronous inputs onto I-M SST^+ neurons? We hypothesized that these interactions are a consequence of network synchronization within preBötC, possibly employing recurrent excitatory connections among these I-M SST^+ neurons as a mechanism[20,21]. This did not appear to be the case, since only one of 50 pairs of preBötC SST^+ neurons, i.e., 2%, were synaptically coupled (Fig. S2a). This led us to postulate that the input synchrony of these neurons results from convergent inputs arising from afferent rhythmogenic neurons, consistent with our previous hypothesis[17]. Putatively rhythmogenic inspiratory preBötC Type-1 neurons (SST^-) interact through excitatory synapses with ~16% probability of any pair having a one-way connection[19]. Notably, in each cycle Type-1 neurons

exhibit a progressive slow increase in their firing rate that starts in preI and continues through the I-burst[22], an AP profile that mirrors the progressive synchronization of EPSPs (from preI to I-bursts) onto I-M SST^+ neurons. Accordingly, among pairs of simultaneously recorded I-M SST^+ neurons, in each cycle there was a significant increase in their V_m correlation associated with the emergence of preI input synchrony (Figs. 2a1-e, S2b1-c3). Importantly, the increase in the V_m correlation was a consequence of short-latency correlated EPSPs during preI and I-bursts (8/90, 23/90 and 35/90 events had <10 ms correlation lags in the IBI, preI and I-burst epochs respectively; Figs. 2b1-b3, d, S2c1-c3); this revealed that input synchrony onto I-M SST^+ neurons represents the synchronization of a preBötC subnetwork generating inspiratory rhythm. Thus, the emergence of periodic synchronous EPSPs in I-M SST^+ neurons (Fig. 1c2) represents a significant spectrotemporal reorganization in the activity of their input population of (presumptive) rhythmogenic neurons. This change in the input structure of I-M SST^+ neurons is a form of preBötC network assembly that only emerges under rhythmic conditions, suggesting that network synchronization is causal to both rhythmogenesis and I-burst generation. Concordantly, when the input synchrony (which we use as a proxy for network synchrony henceforth) onto these neurons was present but weak, there was no resultant I-burst leading to longer IBIs, i.e., intervals between XIIn bursts (Figs. 2f, 4 b,c). Furthermore, the increase in the membrane potential power, signifying an increase in the average frequency of inputs, in non-I-M SST^+ neurons (14/29 neurons; Figs. 2g1-h3, S1c1-c2) was indistinguishable from that of I-M SST^+ neurons (Fig. 2h1-h3), yet input synchrony onto them, i.e., significant increases in spectrotemporal power following periods of uncorrelated activity, was absent (compare Fig. 2f with 2g1-g2; S2d1-d2) further demonstrating synchronized inputs as a necessary condition for I-M SST^+ neuronal activity during I-bursts.

We considered the possibility that this synchrony was an epiphenomenon resulting from increased firing rate of individual neurons, where random alignment of more APs might appear as synchronous input. We tested this computationally in a biophysically realistic neuronal model that had inputs from 10 neurons, each with a Poisson-distributed 2-20 Hz mean AP frequency. We found no indication of any spectrotemporal reorganization from uncorrelated activity to significant input synchrony (Fig. 2i). Moreover, rhythmic bursting was not seen in the physiologically relevant range of input frequencies *in vitro* (each synapse activated at 2-20 Hz mean frequency) (Figs. 2i, S2e). Thus, we conclude that synchrony is not simply the result of an increase in network excitability but a form of network assembly[23] specific to the preBötC rhythm generating

microcircuit, which is necessary for generation of population preI activity and I-bursts that serve as the kernel of inspiratory motor command.

These experiments uncover salient features of preBötC rhythmogenic microcircuit dynamics where simultaneous recordings and assessment of various subpopulation activities revealed dynamic progression of network activity in each inspiratory cycle. To elaborate, the emergence of temporally aligned EPSPs and V_m correlation between I-M SST^+ neurons (Figs. 2 a1-d, S2b1-b4) reflect the onset of output synchrony of their afferent rhythmogenic, including Type-1, neurons. The synchronous firing of I-M SST^+ neurons then leads to I-bursts (Fig. 2e), whereas a decrease in input synchrony results in termination of their AP firing, underlying I-burst termination and initiation of the IBI.

What network mechanism(s) leads to the emergence of preBötC synchrony that appears to underlie rhythmicity? Evidently, an overall uncorrelated increase in the neuronal firing is insufficient (Figs. 2g1-i, S2d1-e). Given that the excitation-inhibition balance in a network is a critical determinant of its output[24], including for breathing[5,8,25,26], we hypothesize that that net impact of increased $[K^+]_{ACSF}$ is to shift the excitation-inhibition balance towards higher excitation, which favors preBötC synchronization. To test this hypothesis, we disinhibited the network by antagonizing gamma-aminobutyric acid type A ($GABA_A$) or glycinergic receptors. To our surprise, the network responses were different. Antagonism of $GABA_A$, but not glycine, receptors in a non-rhythmic slice resulted in rhythmic I-bursts associated with synchronous EPSPs in I-M SST^+ neurons (Figs. 3a1-d2, S3a-f). Strikingly, for I-M SST^+ neurons, at the onset of rhythmic bursting, despite the emergence of input synchrony, their global wavelet power of V_m and their EPSP amplitude, 20%–80% rise times and durations all decreased (Fig. 3e, f-h). In a subset of these experiments where more measurements were recorded (N=6 neurons from 6 slices), in the transition from non-rhythmicity to the emergence of input synchrony and rhythmicity in response to $GABA_AR$ blockade, input resistance (R_{in}) and membrane time constants (τ_m) of these neurons decreased, indicating shift to a higher conductance (HC) state (Fig. 3i-j). This observation presents an unexpected manifestation of efficient cellular and circuit level coordination, where the emergence of synchrony is accompanied by changes in neuronal properties to assure an optimal response[27-29]. Thus, a shift to an HC state changes neuronal integrative properties such that shorter τ_m and increased temporal resolution renders them more responsive to higher frequency inputs thereby favoring coincidence detection and enhancing their response reliability and selectivity to

synchronous inputs[30-35]. This selectivity, especially during preI activity and I-bursts, can facilitate propagation of population activity as synchrony in the subsequent downstream efferent neuronal populations[35-37]. This is evident by the presence of input synchrony in inspiratory phrenic[38] and XII[39] motoneurons during I-bursts.

The observation that antagonizing $GABA_A$ receptors, thus reducing synaptic conductance, leads to an HC state in these preBötC neurons is in contrast to what happens in the neocortex where active inhibitory receptors are instead dominant determinants of an HC state[30]. This led us to explore roles of glycinergic and $GABA_B$ receptors in effectuating HC state in preBötC I-M SST^+ neurons. Thus, when the three types of inhibitory amino acid receptors, i.e., $GABA_A$, $GABA_B$ and glycine, were blocked in 3 mM $[K^+]_{ACSF}$, there was no significant change in the preBötC I-burst frequency compared to $GABA_AR$ blockade only (Fig. 3 k-l), suggesting that network synchronization and rhythmogenesis is exclusively modulated by $GABA_A$ inhibition under these conditions. Furthermore, there was no change in either R_{in} or spontaneous EPSP amplitude (Fig. 3m, 3o). A reduction in the τ_m was also partially reversed as compared to only $GABA_AR$ blockade (Figs. 3n, S3i-j); there was still a significant decrease in EPSP rise time and duration (Fig. 3p-q), suggesting that the integrative neuronal properties may be also regulated by excitatory synaptic and calcium-dependent intrinsic conductances that are active under rhythmic conditions[40]. Furthermore, changes in EPSP rise time and duration were reversible (Fig. 3p, q), ruling out the possibility that the observed changes were primarily due to plasticity in the response dynamics of these neurons with increased network excitability[41]. Taken together, these results uncover a significant and novel dichotomy in the role of GABAergic and glycinergic inhibition in breathing rhythmogenesis. While $GABA_A$ but not glycinergic inhibition regulates synchrony in the network, glycinergic and $GABA_B$ inhibition each can affect mechanisms that shape pattern and assure propagation of I-bursts, as well as affect the IBI. Additionally, our results suggest that antagonizing $GABA_A$ receptors also disinhibits glycinergic inhibition onto I-M SST^+ neurons contributing to an HC state. These observations are direct evidence that network synchronization, irrespective of any significant increase in average population firing rate, is sufficient for preBötC rhythmicity (Fig. 3 d-e). Furthermore, I-M SST^+ neurons can transition to an HC state under 9 mM $[K^+]_{ACSF}$ and associated rhythmicity, possibly as a consequence of increased activity of both excitatory and inhibitory neurons (Fig. S4). This reveals that the network synchronization and increased

conductance state of these neurons are tightly coupled, representing an emergent feature of preBötC microcircuit irrespective of the experimental condition employed to induce rhythmicity.

Given the central role of network synchronization in generation of preBötC I-bursts, we explored its role in their efferent propagation to various motor nuclei that control inspiratory muscles. We noticed that under rhythmic conditions ~16% I-M SST^+ neurons (4/25 neurons recorded in 9 mM $[K^+]_{ACSF}$) received more bouts of synchronous inputs than the number of I-bursts that propagated through XIIn in the same time frame (Figs. 1b2, 2e blue trace,2f, 4a-c). Simultaneous recordings from preBötC and XIIn revealed that when the input synchrony was weak or short-lived (reduced area of significant increase in the V_m power in frequency time plot), preBötC burstlet activity[9] did not propagate to the XIIn. This observation is akin to proposed propagation of network activity in a synfire chain, where propagation of synchronous activity along successive neuronal populations is governed by temporal compactness of population activity and total number of spiking neurons in each population[36,37]. Under such an arrangement, the output synchrony of a given network serves as input synchrony for neurons in the downstream network, so that the stable propagation of population bursts along linear network is a consequence of its input synchrony and total activity of its afferent network[37]. Here, in support of this theory, we find that when the input synchrony onto I-M SST^+ neurons was weak, preBötC I-burst activity either failed to initiate or was truncated as a burstlet (Fig. 4b-c). Additionally, bouts of synchronous EPSPs associated with XIIn I-bursts were sustained for significantly longer that would result in a substantial activity, i.e., I-bursts, compared to those that failed to produce XIIn I-bursts (Fig. 4d-g). Furthermore, a plot of full width half maximum (FWHM) vs amplitude of V_m during input synchrony revealed that successful propagation of preBötC activity was co-dependent on the duration of input synchrony as well as the resultant amplitude of V_m deflections (Fig. 4h), which is a function of temporal compactness as well total activity of the presynaptic population.

Delineating essential features of network dynamics underlying inspiratory rhythmogenesis has been a missing link in the endeavor to understand the neural basis of breathing movements. Here, exploiting a unique experimental preparation where the rhythmogenic kernel is well-defined and whose propagation of rhythmic activity can be tracked to motor nerves, and through direct comparison of network activity under non-rhythmic and rhythmic conditions, we found that network synchronization is essential for I-burst generation and its propagation to motor nerves (Fig. 4i). While synchronous inputs drive each inspiratory cycle, the underlying evolution of EPSP

correlation between I-M SST^+ neurons varies on a cycle to cycle basis (Fig. 2b1-b3), implying that the extent of shared inputs onto these neurons is not fixed, but can vary in each cycle. This suggests that in each cycle the network synchronizes through formation of dynamical cell assemblies[23,42,43]. The variability in the evolution of synchrony in the microcircuit can also manifest as jitter in the preI duration observed in slices (240 ± 10 ms; mean ± sem; range = 63 ms to 588 ms; data for preI events in Fig. 2b1) that marks the onset of network synchronization (also compare Figs. 1c3, 2a and 4c), as well as in the preceding IBIs that reflects the time necessary for the network to assemble. Additionally, given that this preI duration mirrors the latency to induce ectopic I-bursts following synchronous stimulation of very few (3-9) preBötC neurons *in vitro*[10], we hypothesize that this delay reflects the same process where synchronization is seeded by random concurrence in activity of a few neurons that percolates in the preBötC rhythmogenic microcircuit. Similarly, under conditions of reduced network drive, cycle-to-cycle temporal variability in the evolution of network synchrony can contribute to increased jitter in the period of I-bursts[44] (Fig. S3a-b).

Exploring the synaptic mechanisms underlying synchronization, we found that the role of $GABA_A$ergic inhibition in the gating of preBötC synchronization contrasts with its role in promoting synchronous activity in neocortex and other brain regions[24,45-47]. This reveals mechanistic diversity where similar network outputs can be achieved through different synaptic mechanisms, perhaps related to the marked differences in the underlying signal processing and function, i.e., motor control vs. "higher" function. While our study focuses on mechanisms of inspiratory rhythmogenesis, I-burst initiation and propagation, the mechanisms of I-burst termination and control of IBI remain open questions. Given that both burstlets and I-bursts self-terminate, even when all inhibition is blocked (Fig. 3 k,l), we speculate that a decrease in the synaptic efficacy following network synchronization, e.g., due to increased neuronal conductance, contributes to burstlet/burst termination[48]. While not essential to rhythmogenesis, the inhibition originating in the preBötC does regulate the duration of I-bursts, and modulate breathing pattern[5,7,8,25,49].

Furthermore, network synchronization and HC state in the output SST^+ neurons occur concurrently to produce rhythmic bursts. Appearance of such strong association between the network dynamics and neuronal properties to facilitate synchrony transfer[35] is cogent evidence that the inspiratory motor command is a form of temporal neuronal code[23,50]. Moreover, synchrony propagation in the inspiratory motor network (Fig. S5) is seen in the presence of synchronized synaptic inputs onto

medullary inspiratory premotoneurons[51] projecting onto XII[39] and phrenic[38] motoneurons, as well as in the high frequency (HFO; 50-100 Hz) and medium frequency (MFO; 20-50 Hz) oscillations present during inspiration in the: i) discharge patterns of inspiratory premotoneurons and motoneurons[11,13,16,52-54], and; ii) motor nerves projecting to inspiratory muscles[12,13,55].

Finally, in the light of wide scale projections of preBötC SST^+ neurons to other brainstem structures that are modulated by breathing and in turn project to diverse brain regions[11,56,57] and the entrainment of neuronal populations in limbic networks through respiratory corollary discharge[14], we hypothesize the emerging synchronization of preBötC activity in each inspiratory cycle, and its propagation underlie the hypothesized use of breathing rhythms for modulating and/or binding of activity with and across higher brain regions.

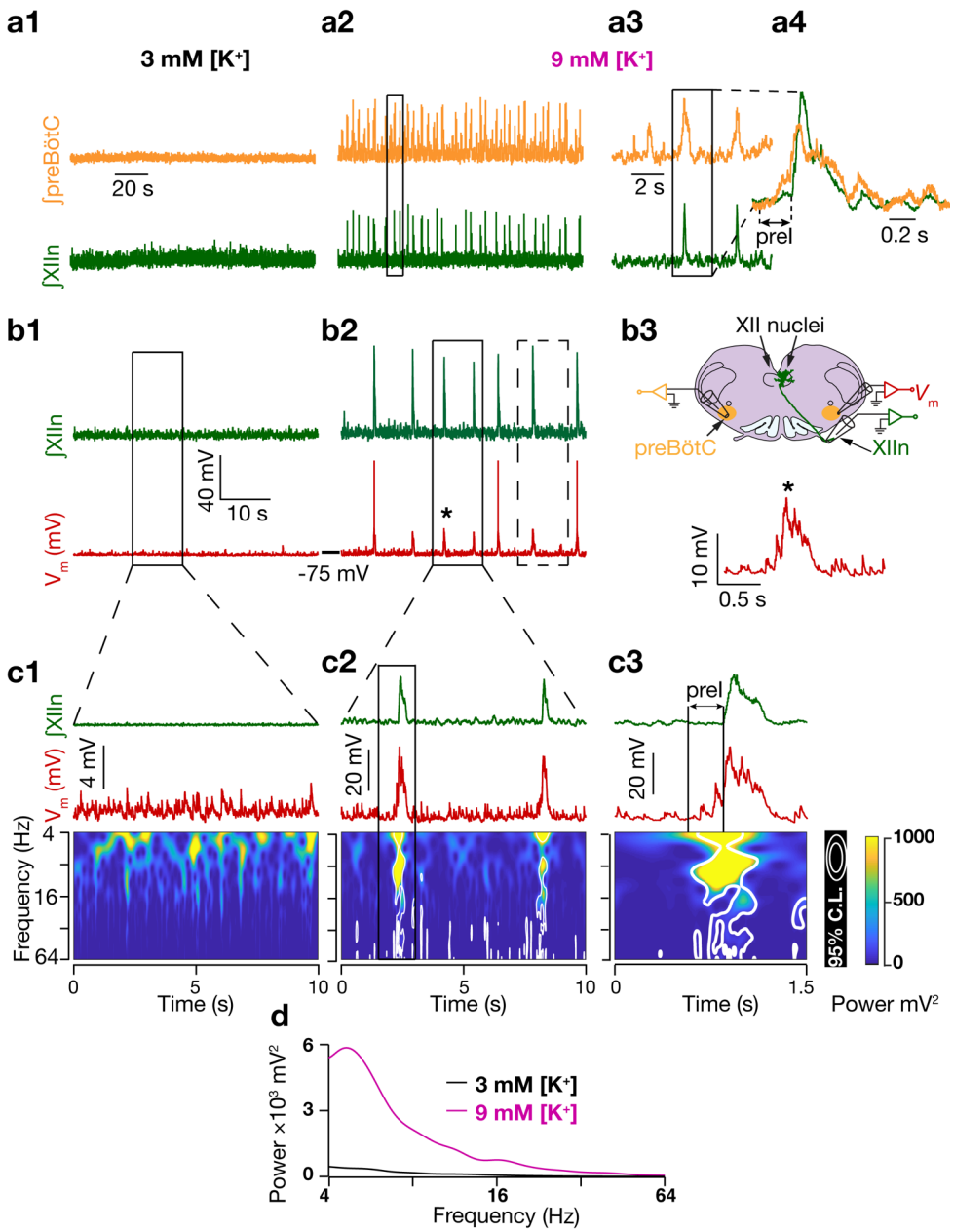

Figure 1. Inputs onto preBötC I-M SST$^+$ neurons undergo spectrotemporal reorganization correlated with the emergence of inspiratory rhythm. **a1-a3**, preBötC population activity (orange top traces: integrated (∫preBötC)); bottom green trace: integrated (∫XIIn)) in 3 mM $[K^+]_{ACSF}$, i.e., control (**a1**), and in 9 mM $[K^+]_{ACSF}$ (**a2**); **a3**, expanded boxed region from (**a2**). **a4**, expanded boxed region from (**a3**) with ∫preBötC and ∫XIIn I-burst overlaid. **b1-b2,** ∫XIIn and I-M SST$^+$ neuron membrane potential (V_m; red trace) in 3 mM $[K^+]_{ACSF}$ (**b1**) and in 9 mM $[K^+]_{ACSF}$ (**b2**); **b3**, top: Cartoon shows recording configuration for simultaneous recording of SST$^+$ neurons in preBötC with XIIn and contralateral preBötC population activity. preBötC neurons project to XII premotor and motor neurons in the slice; bottom: expanded V_m from **b2** marked by *. **c1-c3**, ∫XIIn, V_m and associated frequency-time plot for I-M SST$^+$ neuron in 3 mM $[K^+]_{ACSF}$ (non-rhythmic; **c1;** V_m from solid boxed region in **b1**) and in 9 mM $[K^+]_{ACSF}$ (rhythmic, **c2**; V_m from solid boxed region in **b2**). **c3**, expanded boxed region from **(c2)**. White contours in frequency-time enclose regions where local power was significantly higher (95% confidence level) than the background spectrum, i.e., global wavelet spectrum of V_m in **c1**). Simultaneous ∫XIIn activity is also plotted at the top, notice in c3 the emergence of input synchrony in the preI period well before the emergence of I-burst in the XIIn. **d**, global wavelet spectrum of V_m in **c1** and **c2.**

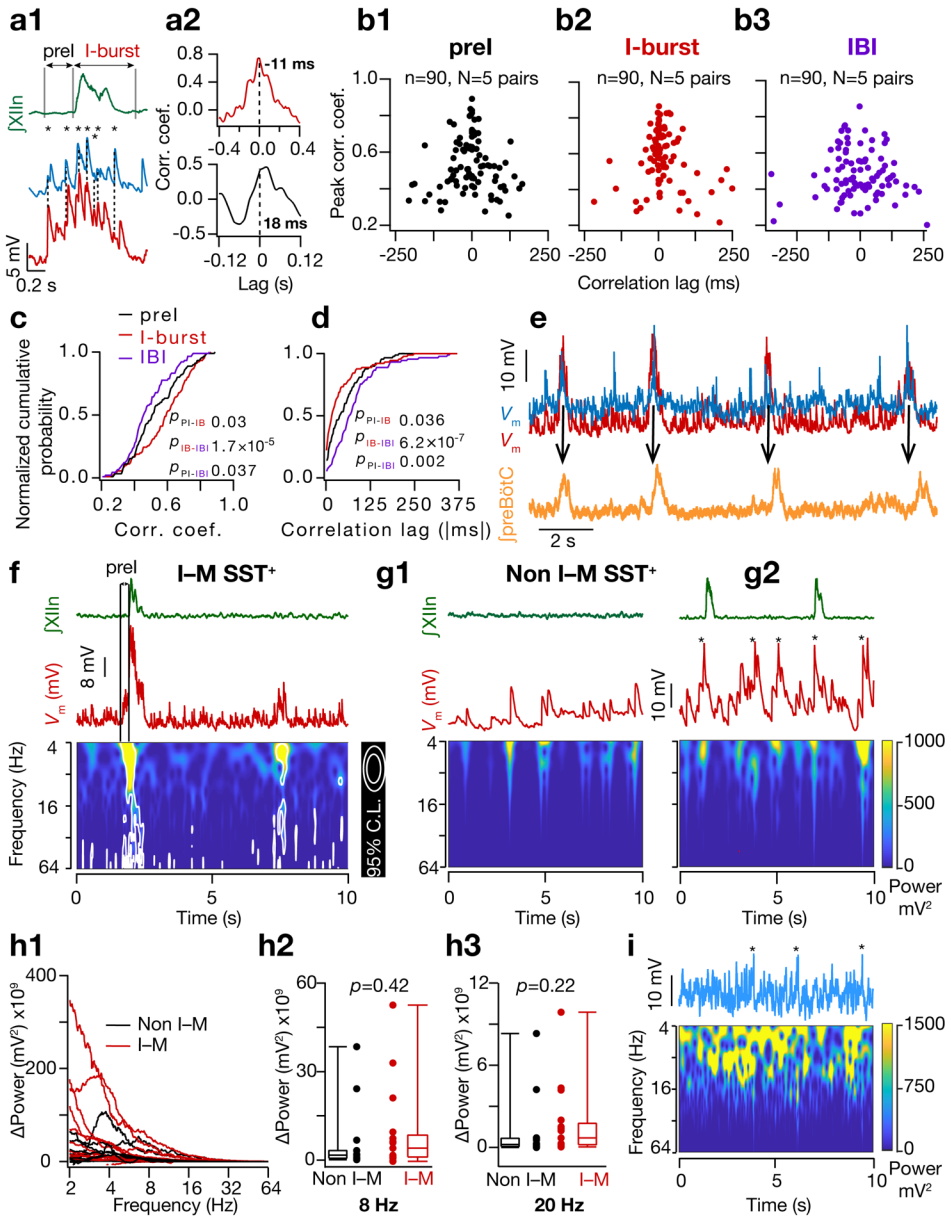

Figure 2. **Input synchrony in I-M SST$^+$ neurons is associated with increased synaptic correlation between neuron pairs during preI and I-bursts. a1**, XIIn and V_m of two simultaneously recorded I-M SST$^+$ neurons along with their cross-correlogram (**a2**) during preI and I-burst. Temporally aligned EPSP peaks indicated by dashed line and *. **b1-b3**, Plots for peak correlation vs time lag for V_m of 5 I-M SST$^+$ pairs (90 cycles from 5 pairs) during preI, I-burst and inter-burst-interval (IBI) epochs. **c-d** normalized cumulative histogram of cross correlation (**c**), and lags (**d**) for events in **b1-b3**. Kruskal Wallis test (**c**, p= 5x10^{-5}; **d**, p= 9x10^{-8}) followed by Wilcoxon signed rank test for pairwise comparisons (p values for color coded pairwise comparisons). **e**, V_m of simultaneously recorded I-M SST$^+$ pair along with ∫preBötC showing that ∫preBötC activity peaks after the peak of V_m in each cycle. **f**, frequency-time plot of V_m of an I-M SST$^+$ neuron (from dashed box region of Fig.1b2) under rhythmic condition showing reduced synchrony during failure of I–burst. **g1-g2**, same as (**f**) but for a non I-M SST$^+$ neuron under control (**g1**) and rhythmic (9mM $[K^+]_{ACSF}$) condition (**g2**). V_m was median filtered to remove APs (indicated by *), **h1- h3**, change in the V_m power of I- and non-I-M SST$^+$ neurons when brainstem slices were shifted from non-rhythmic to rhythmic conditions at various frequencies; p values for Wilcoxon rank sum test. **i**, frequency-time plot of median filtered V_m of a model neuron when 10 excitatory synapses were activated randomly with 15 Hz mean frequency. * indicate filtered APs.

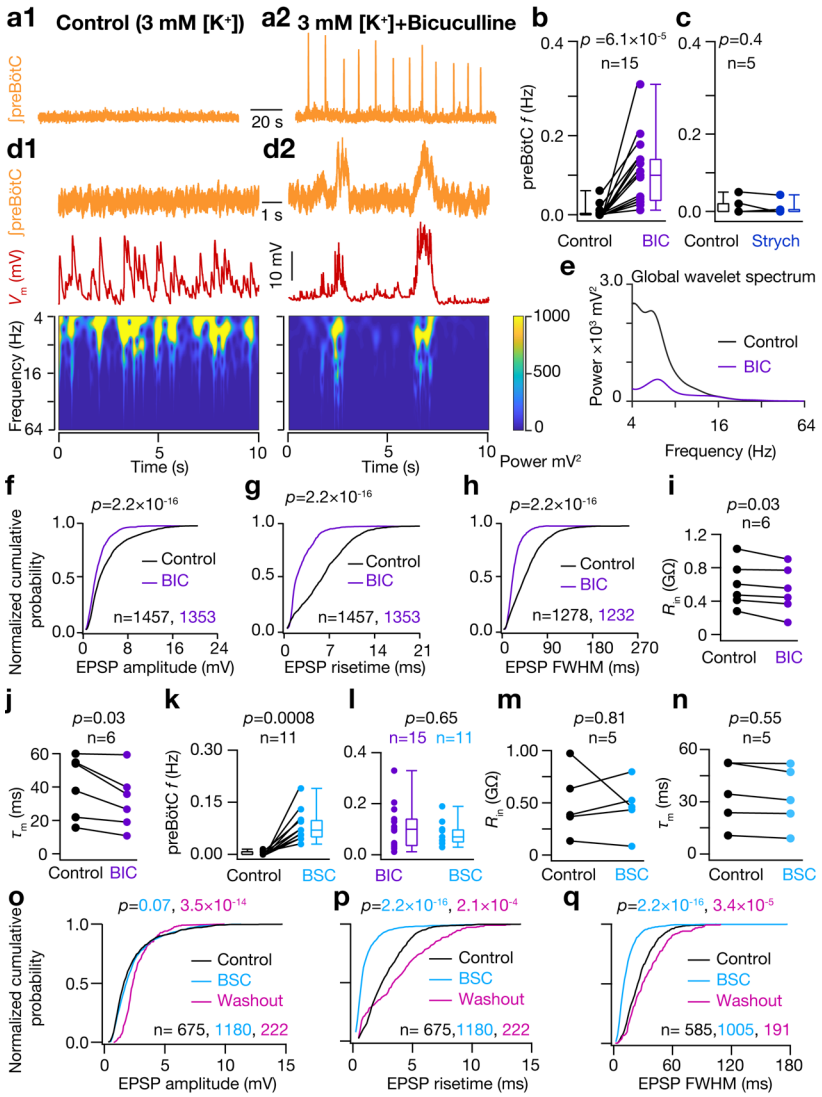

Figure 3. GABA$_A$ inhibition regulates preBötC synchronization and conductance state of I-M SST$^+$ neurons. **a1-a2**, preBötC activity under non-rhythmic, control (**a1**) and under 10 µM Bicuculline (BIC) rhythmic conditions (**a2**). **b-c,** preBötC burst frequency under control and BIC (**b**) and 2 µM strychnine (Strych) (**c**). **d1-d2,** frequency-time plot for V_m of an I-M SST$^+$ neuron under control (**d1**) and rhythmic, BIC, condition (**d2**). **e**, global wavelet spectrum of the V_m in **d1-d2**, note the decrease in global wavelet power under rhythmic conditions with BIC. **f-h**, normalized cumulative probability for spontaneous EPSP amplitude (**f**), 20%-80% rise time (**g**), and full width at half maximum duration, FWHM (**h**), under control (black) and rhythmic condition with BIC in ACSF (purple); N=8 neurons from 8 brain slices. **i**, Input resistance, $R_{in,}$ and membrane time constant, $\tau_{m,}$ (**j**) of I-M SST$^+$ neurons recorded in control and BIC. **k**, preBötC burst frequency recorded under control and with a mixture of 10 µM Bicuculline, 2 µM Strychnine and 2 µM CGP55845 (abbreviated as BSC henceforth) in the ACSF to simultaneously block GABA$_A$, glycinergic and GABA$_B$ receptors respectively. **l**, comparison of preBötC frequency under BIC and BSC conditions. **m-n**, R_{in} (**m**) and τ_m (**n**) of I-M SST$^+$ neurons recorded in control and BSC condition. **o-q,** same as **h-j**, respectively, but under control (black) and BSC (cyan) conditions and after washout of BSC in control ACSF (pink); *p* values for comparison of color-coded experimental sets with the control; N=5 neurons from 5 brain slices. For **b-c** and **k,** *p* values are for Wilcoxon signed rank test; for **f-h**, **l** and **o-q,** *p* values for Wilcoxon rank sum test; for **i-j** and **m-n** *p* values for Wilcoxon signed rank test.

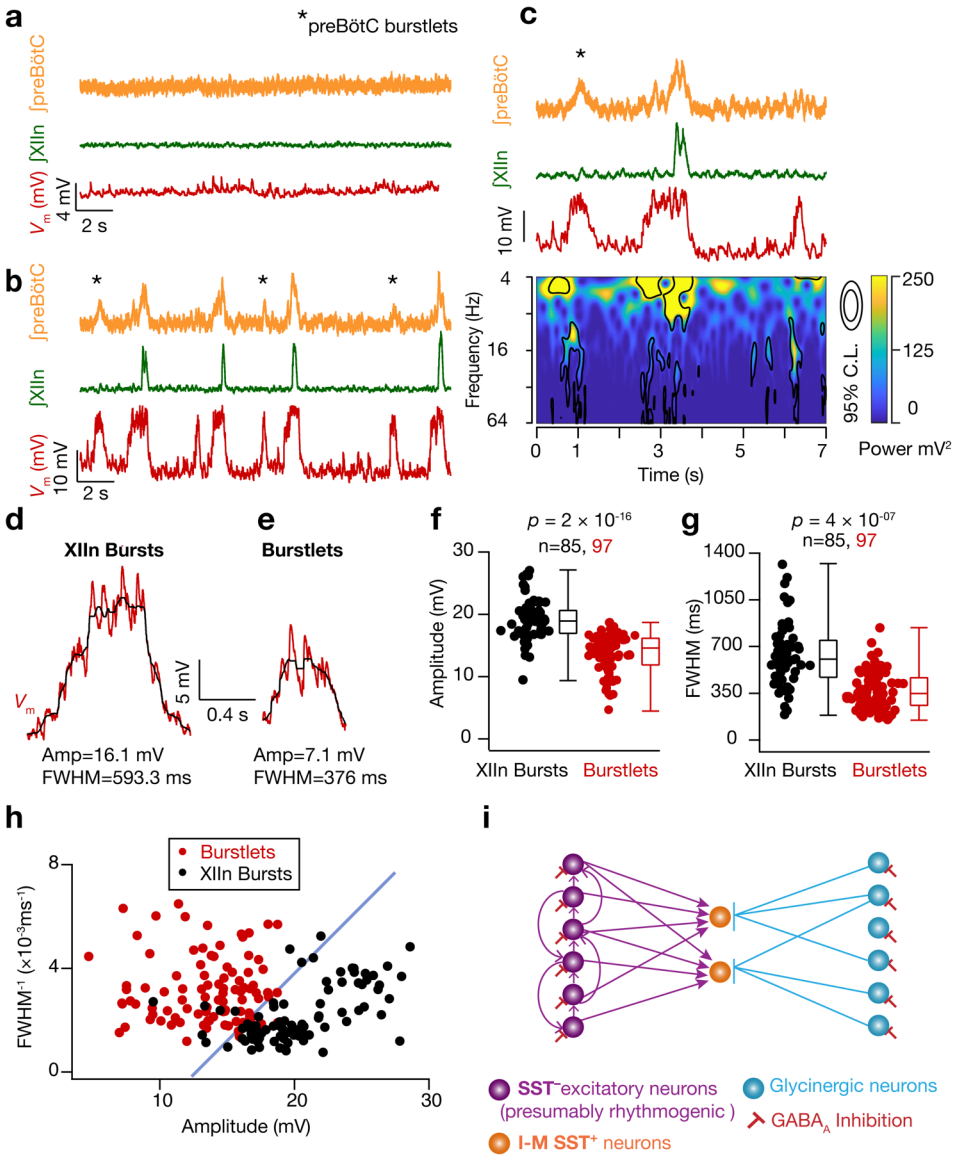

Figure 4. **Propagation of preBötC bursts to XIIn is dependent upon the strength of input synchrony onto I-M SST$^+$ neurons**. **a-b**, simultaneously recorded preBötC and XIIn activity along with V_m of an I-M SST$^+$ neuron recorded under control (**a**) and rhythmic condition with 9 mM $[K^+]_{ACSF}$ (**b**). Notice more bouts of input synchrony in the V_m than preBötC and/or XIIn I-bursts. **c**, frequency-time plot of first 7 seconds from (**b**). **d-e**, representative V_m from another neuron during an I–burst (**d**) and when the input synchrony was not accompanied with an I–burst in XIIn (**e**). Overlaid black traces are median filtered V_m which was used to compute the amplitude and FWHM of V_m deflections during bouts of input synchrony. **f-g**, summary plots for the measurements in **d-e**; n = number of events. **h**, plot of FWHM^{-1} vs amplitude of V_m deflections from I-M SST$^+$ neurons (N=4) during bouts of input synchrony. The data is color coded for synchronous inputs that resulted in XIIn I-bursts (black) and those that did not (red). An arbitrary blue line with slope of 1 ms x mV separates the data into the two groups. **i**, Schematic representation of inputs onto I-M SST$^+$ neurons as inferred from this study. These neurons receive synchronized inputs from SST$^-$ glutamatergic neurons which are presumptively rhythmogenic and connected through excitatory synapses among themselves[19]. I-M SST$^+$ neurons also receive glycinergic inhibition which is also regulated by GABA$_A$ inhibition.

Supplementary Figures

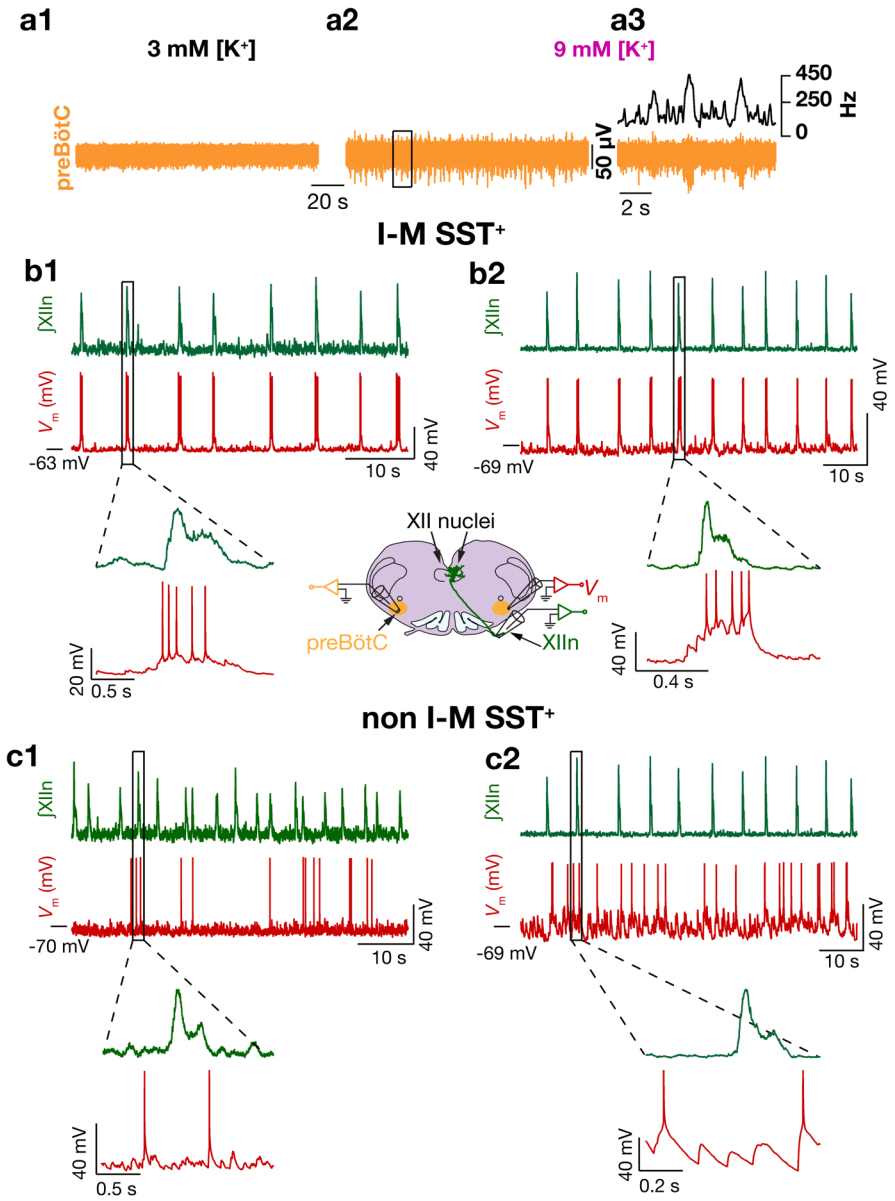

Figure S1. I-M SST$^+$ neurons fire in phase with XIIn I-burst.

a1-a3, preBötC population activity in 3 mM $[K^+]_{ACSF}$, i.e., control (**a1**), and in 9 mM $[K^+]_{ACSF}$ (**a2**); **a3**, expanded boxed region from (**a2**), top black trace is the instantaneous preBötC population firing frequency. **b1-c2**, Firing profiles of I-M SST$^+$ (**b1** & **b2**) and non I-M SST$^+$ (**c1**&**c2**) neurons in 9 mM $[K^+]_{ACSF}$. Cartoon (center) of configuration for simultaneous recording of SST$^+$ neurons in preBötC, XIIn and contralateral preBötC population activity. Traces in **b1** are for the same neuron as in Fig. 1. **b1-c3**. Neurons in **b2** and **c2** were simultaneously recorded in the same rhythmic slice.

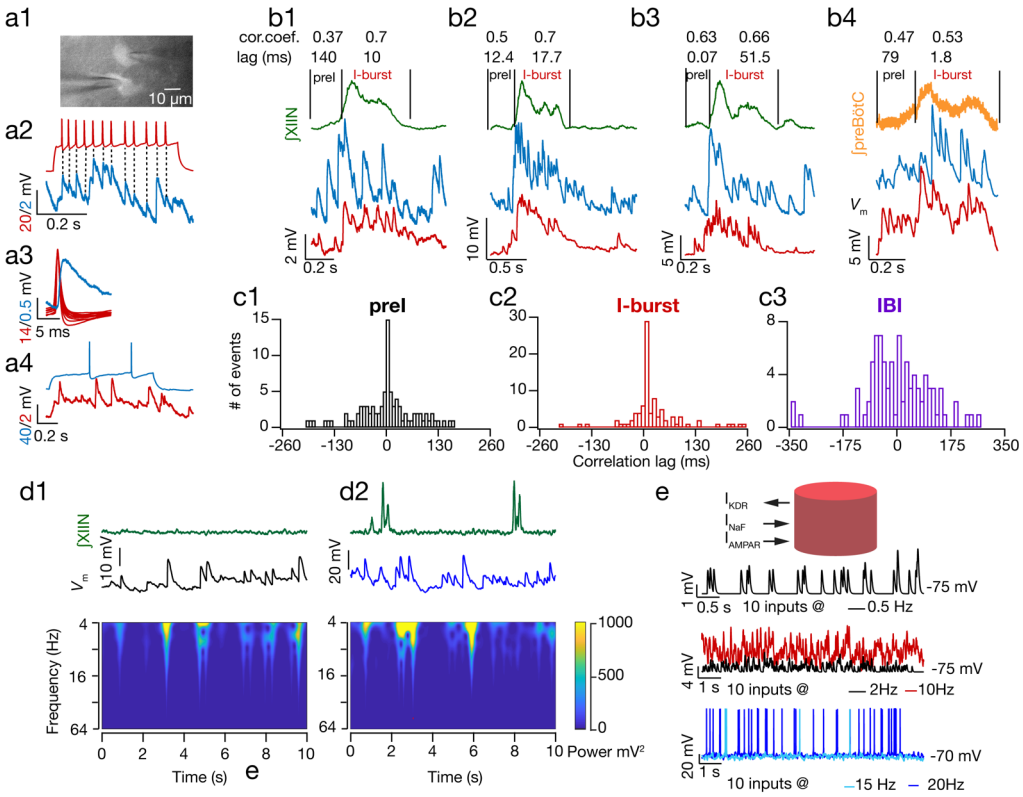

Figure S2. **Specificity and mechanism of input synchrony onto I-M SST$^+$ neurons**. **a1**, Fluorescent micrograph of simultaneously patched SST$^+$ neurons. **a2-a4,** V_m of a synaptically connected pair, represented by red and blue traces, when either of them depolarized to fire action potentials. **a3**, spike triggered average V_m from **a2**. The pair was unidirectionally connected with excitatory synapses, spike-triggered averaged V_m for the connected pair is also shown (middle); EPSP amplitude = 1.7 mV, latency to peak = 3.4 ms. This was the *only* synaptically connected pair among 50 pairs of SST$^+$ neurons tested. **b1-b4**, V_m of four simultaneously recorded I-M SST$^+$ pairs (red, blue) with correlated EPSPs during preI and I-bursts. Traces in **a** and **b1** are from the same pair. Pairs **b2, b3, b4** were not synaptically connected. **c1-c3**, Histogram of cross-correlation lags for V_m of I-M SST$^+$ pairs for the data presented in Fig. 2 **b1-b3** where each point represents an "epoch". **d1-d2**, frequency-time plot of non I-M SST$^+$ neuron same as in Figs. 2 **g1-g2** but when the neuron was not spiking in 9 mM $[K^+]_{ACSF}$. **e**, Representation of a single compartmental biophysical neuronal model with three currents, bottom: V_m under conditions where ten synaptic inputs were randomly activated at various frequencies as indicated.

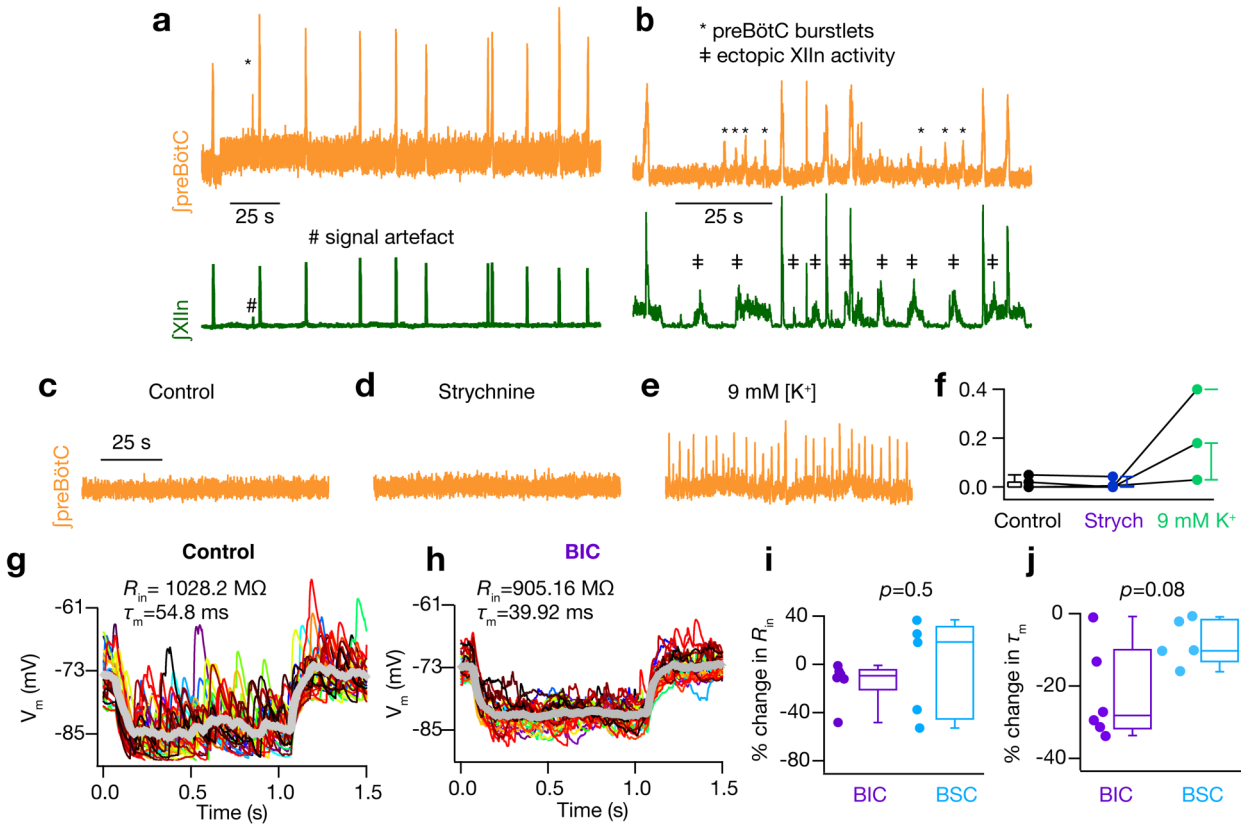

Figure S3. **GABA$_A$ inhibition gates preBötC rhythmogenesis and conductance state of I-M SST$^+$ neurons**. **a-b**, simultaneously recorded preBötC (orange) and XIIn (green) activity in two brainstem slices showing small amplitude preBötC burstlets (marked by *) which did not result in XIIn I-bursts under 10 µM Bicuculline. In some slices, recorded under this condition, ectopic XIIn bursts (**b**; marked ‡) were observed that were not concurrent with preBotC activity and, thus, were not considered for analysis. **c-e**, preBötC activity of a representative slice recorded under control (**c**), 2 µM Strychnine (**d**) and in 9 mM $[K^+]_{ACSF}$ (**e**) after strychnine washout. **f**, same as **Fig. 3c** but with additional experiments depicting activity of 3/5 slices that were also recorded in 9 mM $[K^+]_{ACSF}$ (green) after strychnine washout, e.g., as shown in **c-e**. **g-h**, V_m of an I-M SST$^+$ neurons in response to a hyperpolarizing 10 pA current injection under control (**g**) and under 10 µM Bicuculline (BIC) (**h**), individual traces span 30 trials (depicted by different colors) and thick grey traces are averages under each condition. **i-j**, % change in R_{in} and τ_m of I-M SST$^+$ neurons recorded under BIC and BIC+Strychnine+CGP55845 (BSC) conditions; p values for Wilcoxon rank sum test.

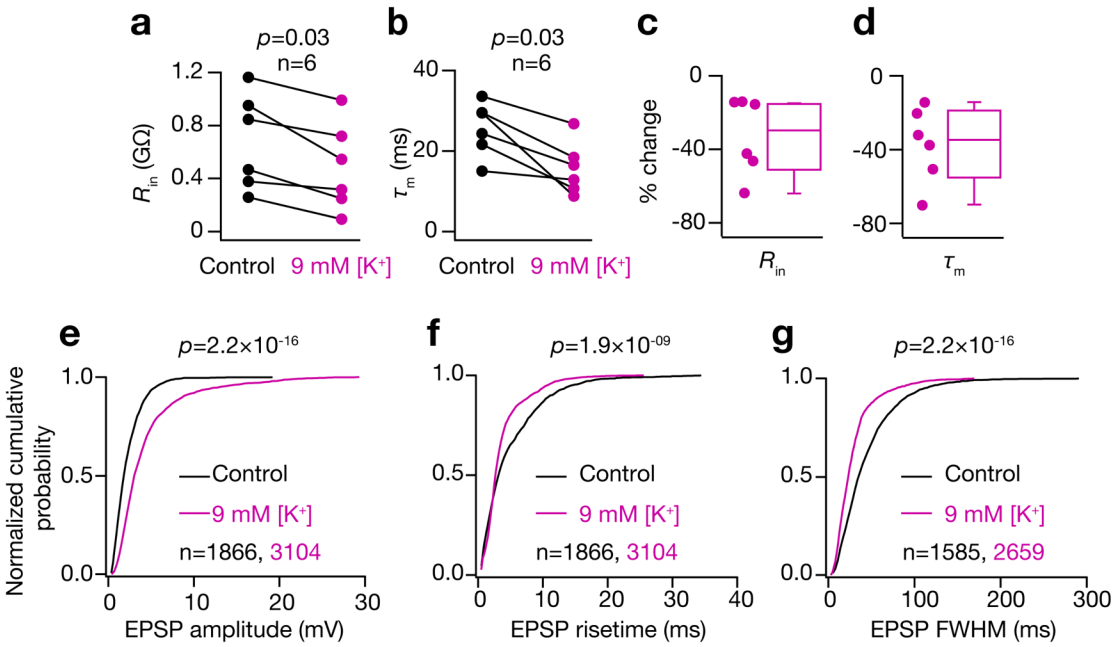

Figure S4. **I-M SST$^+$ neurons shift to higher conductance state in 9 mM [K$^+$]$_{ACSF}$. a,** R_{in}, and **b**) τ_m, of I-M SST$^+$ neurons recorded in control, i.e., 3 mM [K]$_{ACSF}$, and rhythmic 9 mM [K$^+$]$_{ACSF}$ conditions. **c-d**, percentage change in R_{in} and τ_m of these neurons under 9 mM [K$^+$]$_{ACSF}$. **e-g**, normalized cumulative probability of spontaneous EPSP amplitude (**e**), 20%-80% rise time (**f**), and FWHM (**f**) of I-M SST$^+$ neurons in control (black) and rhythmic 9 mM [K$^+$]$_{ACSF}$ (pink) conditions. Note the increase in EPSP amplitude in (**e**) even with a decrease in the gain of these neurons with change of ACSF from control to 9 mM [K$^+$], which could be attributed to an increase in the presynaptic release probability with steady-state depolarization of axon terminals under 9 mM [K$^+$]$_{ACSF}$. **a-b** *p* value for Wilcoxon signed rank test; **c-g** *p* value for Wilcoxon rank sum test. For **e-f** N= number of neurons=14

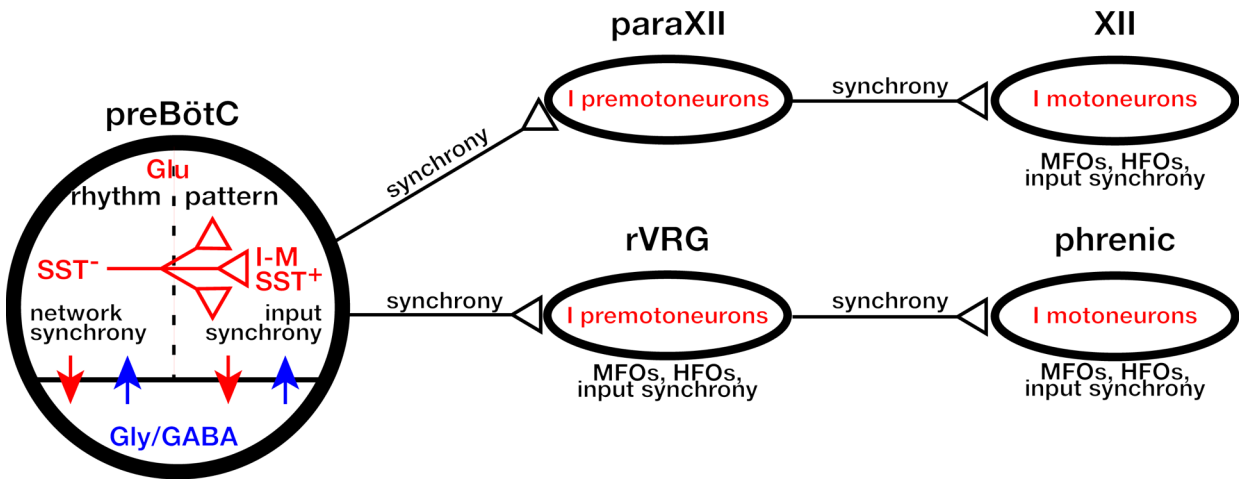

Figure S5. Synchronous propagation of preBötC activity to motor nuclei.

Diagrammatic representation of population activity that emerges as synchrony in preBötC and propagates through inspiratory networks. Synchrony arises from correlated activity of preBötC rhythmogenic neurons and propagates via preBötC output neurons and premotoneurons to inspiratory motoneurons. MFOs = medium frequency (15-50 Hz) oscillations; HFO = High frequency (50-120 Hz) oscillations. Arrows indicate interactions between excitatory (red) and inhibitory (blue) neurons. The schematic is based on data presented in this paper as well as data represented in[11-13,16,38,39,51-55,58].

Methods

Mice

Animal use was in compliance with the guidelines approved by the UCLA Institutional Animal Care and Use Committee. Mice were housed in vivarium with 12-hour light/dark cycle and food and water was supplied ad *libitum*. Adult SST-Cre (IMSR Cat# JAX:013044, RRID: IMSR_JAX:013044) mice were crossed to Ai14 Cre-reporter mice (IMSR Cat# JAX:007914, RRID: IMSR_JAX:007914) to generate the SST reporter line used for *in vitro* slice experiments. All experiments were performed using the reporter line neonates between postnatal 0 to postnatal 7 days old.

In Vitro slice preparation and electrophysiological recordings.

The neuraxis containing the brainstem and the spinal cord, from neonatal mice of either sex, was isolated and one transverse brainstem slice (550 µm-600 µm thick) was prepared from each animal that contained the preBötC along with respiratory premotor and hypoglossal (XII) respiratory motor neurons and XII nerve (XIIn) rootlets. The slice was cut (using a Leica VT1200 slicer) such that the preBötC was on the surface of the slice when placed rostral side facing upwards and contained anatomical landmarks as described in[59]. The slices were cut in chilled ACSF containing (in mM): 124 NaCl, 3KCl, 1 $MgSO_4$, 25 $NaHCO_3$, 0.5 NaH_2PO_4 and 30 D-glucose, bubbled with 95%CO_2 and 5% O_2, at 7.4 pH

For electrophysiological recordings, slices were perfused with ACSF (32-34˚C) at 4 ml/min in the recording chamber where they were allowed to recover for at least 30 minutes in normal ACSF before the start of recordings. To record preBötC and XIIn population activity, ACSF filled suction electrodes were used (with ~150 µm tip diameter) pulled from borosilicate glass (1.2 mm outer diameter with 0.52 mm wall thickness) using P-97 puller from Sutter Instruments. Data was acquired through a differential AC amplifier (A-M Systems, Model 1700), filtered at 1-5 kHz and digitalized using a MultiClamp 700B (Molecular Devices). The sampling frequency was either 20 or 40 kHz. The population recording time series was full wave rectified and integrated using a custom built analog Paynter filter with a time constant of 15 ms. The integrated data lacked scale for comparisons across experiments and, thus, was represented as normalized arbitrary units[9].

For intracellular whole-cell current-clamp clamp recordings, fluorescently labeled (tdTomato) somatostatin-positive (SST^+) neurons were patched under visually guided video microscopy using an upright microscope (either Zeiss Examiner A1or Olympus BX51W1) fitted with DIC optics and CCD camera (Andor Technology iXon or Hamamatsu C11440). The preBötC boundary was ventral to nucleus ambiguous and lateral to the principle loop of inferior olive. Neurons were patched with glass electrodes of ~1 µm tip diameter with electrode resistance of 5-8 MΩ. Electrodes were pulled from borosilicate glass capillary (1.5 mm outer diameter, 0.64 mm wall thickness) using P-97 microelectrode puller (Sutter Instruments) and filled with intracellular solution containing (in mM): 120 K-gluconate, 20 KCl,10 HEPES, 4 NaCl, 4 Mg-ATP,0.3 Na-GTP, and 7 K_2-phosphocreatine (pH= 7.3 adjusted with KOH, osmolarity ~310 mOsm). Whole-cell current-clamp recordings were performed on SST^+ neuronal somata using Dagan IX2-700 amplifier and data was digitalized using a MultiClamp 700B at either 20 or 40 kHz. Measured liquid junction potential (LJP) between the pipette solution and ACSF was 16-20 mV and it was not compensated during the experiment. Unless otherwise noted, all neurons were hyperpolarized to ~–75 mV by negative current injection to record synaptic inputs and minimize their AP firing. Resting membrane potential at break-in (without LJP compensation) was between –48 mV to –60 mV. Series resistance (R_s) and series capacitance (C_s) was monitored by examining the voltage response of the patched neurons to a hyperpolarizing current injection of 10 pA and was compensated online through bridge balance, though high synaptic noise and hence fluctuating membrane potential meant that the compensation was only approximate. R_s range was between 13 MΩ-40 MΩ.

Pharmacology. To block γ-aminobutyric acid (GABA) type A receptors ($GABA_AR$), glycine receptors (GlyR) and $GABA_B$ receptors 10 µM (-)Bicuculline methiodide (Tocris Bioscience), 2 µM Strychnine hydrochloride (Tocris Bioscience) and 2 µM CGP55845 (Tocris Bioscience) were used respectively.

To induce inspiratory rhythm in preBötC slices either $[K^+]_{ACSF}$ was increased to 9 mM or inhibition was pharmacologically blocked in normal, i.e., 3 mM $[K^+]_{ACSF}$.

Simulations. A biophysically realistic conductance based single-compartmental model of preBötC neuron was constructed as a cylinder 20 µm in diameter and 20 µm long with the following passive parameters: membrane capacitance, C_m = 1 µF/cm^2; specific membrane resistance

(R_m) = 10 MΩ.cm^2 and axial resistivity (R_a) = 200 Ω.cm. These parameters were chosen such that the input resistance, R_{in}, of the model neuron was 350 MΩ, which falls in the range of experimentally observed values of R_{in} for I-M SST$^+$ neurons (Figs. 3i and 3m). Two voltage-gated ion channels, i.e., a fast sodium (NaF) and a delayed rectifier potassium (KDR), were incorporated into the model. Each ion channel was modeled using a Hodgkin-Huxley formulation adopted from[60]. NaF channel density was 45 mS/cm^2 and KDR channel density was 15 mS/cm^2. Current through α-amino-3-hydroxy-5-methyl-4-isoxazolepropionic acid (AMPA) receptors was modeled as a combination of sodium and potassium currents:

$$I_{AMPA}(v,t) = I_{AMPA}^{Na}(v,t) + I_{AMPA}^{K}(v,t) \quad \text{.....(...8)}$$

where,

$$I_{AMPA}^{Na}(v,t) = \bar{P}_{AMPA}\, P_{Na} s(t) \times \frac{vF^2}{RT}\left(\frac{[Na]_i - [Na]_o exp\left(-\frac{vF}{RT}\right)}{1 - exp\left(-\frac{vF}{RT}\right)}\right) \quad \text{.....(9)}$$

$$I_{AMPA}^{K}(v,t) = \bar{P}_{AMPA}\, P_{K} s(t) \times \frac{vF^2}{RT}\left(\frac{[K]_i - [K]_o exp\left(-\frac{vF}{RT}\right)}{1 - exp\left(-\frac{vF}{RT}\right)}\right) \quad \text{.....(10)}$$

where $\bar{P}_{AMPA}$ is the maximum permeability of AMPAR that was set to 1x10^{-7} cm/s so that the resultant EPSP amplitude was 2.5 mV, which approximates the mean amplitude of spontaneous EPSPs of I-M SST$^+$ neurons under normal ACSF (Figs. 3f and 3o). P_{Na} was set equal to P_K=1 [61]. $s(t)$ determined the kinetics of current through AMPAR and was defined as:

$$s(t) = a\left(exp\left(-\frac{t}{\tau_d}\right) - exp\left(-\frac{t}{\tau_r}\right)\right) \quad \text{.....(11)}$$

where a is a normalization constant to ensure that $0 \leq s(t) \leq 1$. τ_r=2 ms and τ_d=10 ms[62].

All simulations were performed in the *NEURON* simulation environment[63] with the integration time step of 25 µs. Resting membrane potential was set at -75 mV, simulation temperature was 34˚C and ion channel kinetics were adjusted per their experimentally determined Q_{10} coefficients.

Data analysis. To estimate input resistance, R_{in}, a hyperpolarizing pulse of 10 pA current pulse of 1s duration was applied for 10-30 trials (Fig. S3 g-h). The average membrane potential deflection was then divided by the injected current to get the estimate of R_{in}. To compute membrane time constant, τ_m, the repolarizing phase of the averaged V_m trace was fitted with an exponential function of form:

$$y_0+A\exp[-(x-x_0)/\ \tau_m]; \ldots\ldots\ldots\ldots\ldots\ldots\ldots\ldots\ldots(1)$$

where y_0, A and τ_m are fit coefficients and x_0 is the steady-state value of V_m at the end of repolarization. For these estimates, only trials in the interburst intervals were considered.

To compute population firing rate from population recordings (Fig. S1 a3) raw signal was first band-pass filtered between 300 Hz to 3 kHz to get multiunit activity (MUA). From this MUA, extracellular action potentials, exhibiting positive and negative polarity, were detected as peaks that were greater than a predetermined threshold in either direction and were separated from each other by at least 1.5 ms (to avoid multiple detection of same spike). The threshold for spike detection was determined by the noise level (representing neuronal + signal noise) present under the non-rhythmic condition (in normal ACSF) and in this case (Fig. S1 a3) was set to 10 µV. Spike times of detected spikes was converted into instantaneous firing frequency which was then box smoothened twice, with a window of 2 ms, to give rise to the final population firing rate trace.

Wavelet analysis. Time frequency decomposition of neuronal V_m by continuous wavelet transform (CWT) was implemented through guidelines presented in[64]. Briefly, V_m was subtracted from its mean and normalized by its standard deviation. Thereafter, CWT was performed on the resultant time series, x_n, defined as the convolution of x_n with scaled and translated version of the wavelet function $\Psi_0(\eta)$:

$$W_n(s) = \sum_{n'=0}^{N-1} x_{n'}\psi * \left[\frac{(n'-n)\delta t}{s}\right]\ldots\ldots\ldots\ldots(2)$$

where the (*) indicates complex conjugate. The minimum scale, s_0, was fixed at 0.0153 s (corresponding to 64 Hz). Subsequent scales were determined as:

$$s_j=s_0*2^{j\partial j}, j=0,1,\ldots,J\ldots\ldots\ldots\ldots\ldots\ldots\ldots\ldots(3)$$

$$J=7/\partial j \ldots\ldots\ldots\ldots\ldots\ldots\ldots\ldots\ldots\ldots\ldots\ldots(4)$$

Where, J determined the largest scale and ∂j , i.e., increment of J, was fixed at 0.025. Thus, the total number of scales was J+1= 281. Ψ is the normalized version of $\Psi_0(\eta)$ which is the complex Morlet wavelet defined as:

$$\psi_0(\eta) = \pi^{-1/4} e^{i\omega_0 \eta} e^{-\eta^2/2} \quad \ldots\ldots\ldots\ldots(5)$$

Where ω_0 is the nondimensional frequency chosen to be 6 to satisfy the admissibility criterion for a Morlet wavelet[64]. η is the nondimensional time parameter. $\Psi_0(\eta)$ was normalized to give Ψ so that at each scale, s, the wavelet function has unit energy irrespective of the scale size:

$$\hat{\psi}(s\omega_k) = \left(\frac{2\pi s}{\delta t}\right) \hat{\psi}_0(s\omega_k) \ldots\ldots\ldots\ldots\ldots\ldots(6)$$

This made it possible to directly compare the wavelet transform at each scale and to the wavelet transforms of other time series[64], i.e., wavelet transforms of V_m of a given neuron under inspiratory rhythmic and non-rhythmic conditions. The global wavelet spectrum was computed as the time averaged wavelet spectrum over entire time multiplied by the variance of the original signal. For significance testing the global wavelet spectrum of V_m under non-rhythmic condition (normal ACSF) was chosen as background spectrum for each neuron. Peaks in the wavelet spectrum of the V_m of the same neuron under rhythmic condition was then considered to be above the background spectrum with 5% significance level (or 95% confidence level) if it was above the product of background spectrum with 95th percentile value for chi-square distribution having two degrees of freedom[64]. Wavelet software was provided by C. Torrence and G. Compo: http://paos.colorado.edu/research/wavelets/.

Unless otherwise stated, only epochs of V_m without any APs were used in the analysis. When V_m containing APs was used, they were removed through median filtering in a two-step process. First, in a large window of 10-13 ms all data points greater than 3 mV from the median were replaced by the median. This selectively removed AP peaks with sharp transients at the base of the truncated APs. The filtered signal was again median filtered with a 2 ms window to remove these transients. This process ensured that only APs were removed from the V_m trace without distorting synaptic

potentials. To get the envelop of V_m deflections during the epochs of synchronous inputs (Fig. 4 d-h) the traces were median filtered with a 25 ms window.

For paired whole-cell patch-clamp recordings, fluorescently labelled SST^+ neuronal pairs were patched at intersomatic distance of 10-100 µm. The normalized cross-correlation between two time series, *x(t)* and *y(t)* (V_m of paired neurons for our analysis), was calculated as follows[65]:

$$c_{xy}(\tau) = \frac{1}{N}\frac{\sum_{t=0}^{L}(x(t)-\bar{x})\,(y(t+\tau)-\bar{y})}{\sigma_x\sigma_y} \quad \ldots\ldots\ldots\ldots\ldots\ldots(7)$$

where, L is the total length of the signal, $\bar{x}$ *and* $\bar{y}$ *and* σ_x *and* σ_y are means and standard deviations of *x(t)* and *y(t)* respectively. The value of $c_{xy}(\tau)$ varies from -1 to 1 such that two identical signals will have a value of 1 at zero time lag ($\tau = 0$). PreI duration was determined as the time between the onset of preBötC activity and the onset of an I-burst in the XIIn. The onset of preBötC activity was determined by the start of positive inflection in the differentiated ∫preBötC_trace. For one I-M SST^+ pair XIIn was not active, hence the preI period was determined by the initial slope of ∫preBötC trace (Fig. S2 b4)[9]. Epochs of inter burst intervals (IBI) extracted from V_m trace were ~1 second after the termination of the I-burst given that they did not overlap with preBötC burstlets. For direct comparison, the duration of IBI epochs was fixed at the duration of the preI period preceding it.

To probe synaptic connections between the recorded neurons, a depolarizing current pulse was injected sequentially in each neuron to produce APs. The spike triggered average of V_m in non-firing neurons was computed to ascertain synaptic connectivity.

For quantification of spontaneous excitatory postsynaptic potentials (EPSPs), 100-300 s epochs of V_m from I-M SST^+ neurons were used. Custom semi-automated peak detection software was used to select for spontaneous EPSPs. Due to very high synaptic noise, the start and end of each EPSP was manually specified to avoid temporally clustered EPSPs being falsely detected as a unitary EPSP. Only those EPSPs which did not have any visually detectable inflections in their rising phase were considered for analysis. When there were overriding EPSPs in the decay phase of a selected EPSP, its full width at half maximal (FWHM) duration was not computed. This resulted in a reduced number of events that were analyzed for FWHM as compared to EPSPs amplitude

and rise time (*cf.* Figs. 3 f-h and 3 o-q). EPSP amplitude was defined as the difference of peak V_m from the baseline value for each event. 20%-80% rise time was defined as the duration in which the EPSP grew from 20% to 80% of peak amplitude. For non-I-M SST^+ neurons, the recording duration was shorter and hence 50-100 s epochs were used for EPSP analysis.

Data was analyzed using custom software in Igor Pro (version 7.4; WaveMetrics Inc.). Statistical analyses were performed using R software (www.r-project.org). Sample size was not predetermined. Normality was neither tested nor assumed and hence, for statistical testing, non-parametric tests were used. For box-and-whisker plots, center line represents the median; box limits, upper and lower quartiles and whiskers represent 90 and 10 percentile range.

References

1 Smith, J. C., Ellenberger, H. H., Ballanyi, K., Richter, D. W. & Feldman, J. L. Pre-Botzinger complex: a brainstem region that may generate respiratory rhythm in mammals. *Science* **254**, 726-729 (1991).

2 Del Negro, C. A., Funk, G. D. & Feldman, J. L. Breathing matters. *Nat Rev Neurosci* **19**, 351-367, doi:10.1038/s41583-018-0003-6 (2018).

3 Rekling, J. C. & Feldman, J. L. PreBotzinger complex and pacemaker neurons: hypothesized site and kernel for respiratory rhythm generation. *Annu Rev Physiol* **60**, 385-405, doi:10.1146/annurev.physiol.60.1.385 (1998).

4 Feldman, J. L., Del Negro, C. A. & Gray, P. A. Understanding the rhythm of breathing: so near, yet so far. *Annu Rev Physiol* **75**, 423-452, doi:10.1146/annurev-physiol-040510-130049 (2013).

5 Janczewski, W. A., Tashima, A., Hsu, P., Cui, Y. & Feldman, J. L. Role of inhibition in respiratory pattern generation. *J Neurosci* **33**, 5454-5465, doi:10.1523/JNEUROSCI.1595-12.2013 (2013).

6 Feldman, J. L. & Kam, K. Facing the challenge of mammalian neural microcircuits: taking a few breaths may help. *J Physiol* **593**, 3-23, doi:10.1113/jphysiol.2014.277632 (2015).

7 Sherman, D., Worrell, J. W., Cui, Y. & Feldman, J. L. Optogenetic perturbation of preBotzinger complex inhibitory neurons modulates respiratory pattern. *Nat Neurosci* **18**, 408-414, doi:10.1038/nn.3938 (2015).

8 Baertsch, N. A., Baertsch, H. C. & Ramirez, J. M. The interdependence of excitation and inhibition for the control of dynamic breathing rhythms. *Nat Commun* **9**, 843, doi:10.1038/s41467-018-03223-x (2018).

9 Kam, K., Worrell, J. W., Janczewski, W. A., Cui, Y. & Feldman, J. L. Distinct inspiratory rhythm and pattern generating mechanisms in the preBotzinger complex. *J Neurosci* **33**, 9235-9245, doi:10.1523/JNEUROSCI.4143-12.2013 (2013).

10 Kam, K., Worrell, J. W., Ventalon, C., Emiliani, V. & Feldman, J. L. Emergence of population bursts from simultaneous activation of small subsets of preBotzinger complex inspiratory neurons. *J Neurosci* **33**, 3332-3338, doi:10.1523/JNEUROSCI.4574-12.2013 (2013).

11 Yang, C. F. & Feldman, J. L. Efferent projections of excitatory and inhibitory preBotzinger Complex neurons. *J Comp Neurol* **526**, 1389-1402, doi:10.1002/cne.24415 (2018).

12 Funk, G. D. & Parkis, M. A. High frequency oscillations in respiratory networks: functionally significant or phenomenological? *Respir Physiol Neurobiol* **131**, 101-120 (2002).

13 Christakos, C. N., Cohen, M. I., Barnhardt, R. & Shaw, C. F. Fast rhythms in phrenic motoneuron and nerve discharges. *Journal of neurophysiology* **66**, 674-687, doi:10.1152/jn.1991.66.3.674 (1991).

14 Karalis N, S. B. Breathing coordinates limbic network dynamics underlying memory consolidation. *bioRxiv*, doi: http://dx.doi.org/10.1101/392530. (2018).

15 Stornetta, R. L. *et al.* A group of glutamatergic interneurons expressing high levels of both neurokinin-1 receptors and somatostatin identifies the region of the pre-Botzinger complex. *J Comp Neurol* **455**, 499-512, doi:10.1002/cne.10504 (2003).

16 Tan, W., Pagliardini, S., Yang, P., Janczewski, W. A. & Feldman, J. L. Projections of preBotzinger complex neurons in adult rats. *J Comp Neurol* **518**, 1862-1878, doi:10.1002/cne.22308 (2010).
17 Cui, Y. *et al.* Defining preBotzinger Complex Rhythm- and Pattern-Generating Neural Microcircuits In Vivo. *Neuron* **91**, 602-614, doi:10.1016/j.neuron.2016.07.003 (2016).
18 Tan, W. *et al.* Silencing preBotzinger complex somatostatin-expressing neurons induces persistent apnea in awake rat. *Nat Neurosci* **11**, 538-540, doi:10.1038/nn.2104 (2008).
19 Rekling, J. C., Shao, X. M. & Feldman, J. L. Electrical coupling and excitatory synaptic transmission between rhythmogenic respiratory neurons in the preBotzinger complex. *J Neurosci* **20**, RC113 (2000).
20 Miles, R. & Wong, R. K. Excitatory synaptic interactions between CA3 neurones in the guinea-pig hippocampus. *J Physiol* **373**, 397-418 (1986).
21 Guzman, S. J., Schlogl, A., Frotscher, M. & Jonas, P. Synaptic mechanisms of pattern completion in the hippocampal CA3 network. *Science* **353**, 1117-1123, doi:10.1126/science.aaf1836 (2016).
22 Gray, P. A., Rekling, J. C., Bocchiaro, C. M. & Feldman, J. L. Modulation of respiratory frequency by peptidergic input to rhythmogenic neurons in the preBotzinger complex. *Science* **286**, 1566-1568 (1999).
23 Buzsaki, G. & Draguhn, A. Neuronal oscillations in cortical networks. *Science* **304**, 1926-1929, doi:10.1126/science.1099745 (2004).
24 Bartos, M. *et al.* Fast synaptic inhibition promotes synchronized gamma oscillations in hippocampal interneuron networks. *Proc Natl Acad Sci U S A* **99**, 13222-13227, doi:10.1073/pnas.192233099 (2002).
25 Baertsch, N. A., Severs, L. J., Anderson, T. M. & Ramirez, J. M. A spatially dynamic network underlies the generation of inspiratory behaviors. *Proc Natl Acad Sci U S A* **116**, 7493-7502, doi:10.1073/pnas.1900523116 (2019).
26 Xiaolu Sun, C. T. P., D Nagaraj Halemani, Xuesi M. Shao, Morgan Greenwood, Sarah Heath, Jack L. Feldman, Kaiwen Kam. *bioRxiv*, doi:https://doi.org/10.1101/665034 (2019).
27 Barlow, H. B. in *Sensory communication* (ed W.A. Rosenblith) 217-234 (The MIT Press, 1961).
28 Deneve, S., Alemi, A. & Bourdoukan, R. The Brain as an Efficient and Robust Adaptive Learner. *Neuron* **94**, 969-977, doi:10.1016/j.neuron.2017.05.016 (2017).
29 Das, A. & Narayanan, R. Theta-frequency selectivity in the somatic spike triggered average of rat hippocampal pyramidal neurons is dependent on HCN channels. *Journal of neurophysiology* **118**, 2251-2266, doi:10.1152/jn.00356.2017 (2017).
30 Destexhe, A., Rudolph, M. & Pare, D. The high-conductance state of neocortical neurons in vivo. *Nat Rev Neurosci* **4**, 739-751, doi:10.1038/nrn1198nrn1198 [pii] (2003).
31 Fernandez, F. R., Broicher, T., Truong, A. & White, J. A. Membrane voltage fluctuations reduce spike frequency adaptation and preserve output gain in CA1 pyramidal neurons in a high-conductance state. *J Neurosci* **31**, 3880-3893, doi:10.1523/JNEUROSCI.5076-10.2011 (2011).
32 Stevens, C. F. & Zador, A. M. Input synchrony and the irregular firing of cortical neurons. *Nat Neurosci* **1**, 210-217, doi:10.1038/659 (1998).
33 Contreras, D. & Steriade, M. Spindle oscillation in cats: the role of corticothalamic feedback in a thalamically generated rhythm. *J Physiol* **490 (Pt 1)**, 159-179 (1996).

34 Rudolph, M. & Destexhe, A. A fast-conducting, stochastic integrative mode for neocortical neurons in vivo. *J Neurosci* **23**, 2466-2476 (2003).
35 Ratte, S., Hong, S., De Schutter, E. & Prescott, S. A. Impact of neuronal properties on network coding: roles of spike initiation dynamics and robust synchrony transfer. *Neuron* **78**, 758-772, doi:10.1016/j.neuron.2013.05.030 (2013).
36 Kumar, A., Rotter, S. & Aertsen, A. Spiking activity propagation in neuronal networks: reconciling different perspectives on neural coding. *Nat Rev Neurosci* **11**, 615-627, doi:10.1038/nrn2886 (2010).
37 Diesmann, M., Gewaltig, M. O. & Aertsen, A. Stable propagation of synchronous spiking in cortical neural networks. *Nature* **402**, 529-533, doi:10.1038/990101 (1999).
38 Parkis, M. A., Feldman, J. L., Robinson, D. M. & Funk, G. D. Oscillations in endogenous inputs to neurons affect excitability and signal processing. *J Neurosci* **23**, 8152-8158 (2003).
39 Wang, J. *et al.* Synaptic activation of hypoglossal respiratory motorneurons during inspiration in rats. *Neurosci Lett* **332**, 195-199 (2002).
40 Del Negro, C. A. *et al.* Synaptically activated burst-generating conductances may underlie a group-pacemaker mechanism for respiratory rhythm generation in mammals. *Prog Brain Res* **187**, 111-136, doi:10.1016/B978-0-444-53613-6.00008-3 (2010).
41 Narayanan, R., Dougherty, K. J. & Johnston, D. Calcium Store Depletion Induces Persistent Perisomatic Increases in the Functional Density of h Channels in Hippocampal Pyramidal Neurons. *Neuron* **68**, 921-935, doi:S0896-6273(10)00975-X [pii]10.1016j.neuron2010.11.033 (2010).
42 Tsukada, M., Ichinose, N., Aihara, K., Ito, H. & Fujii, H. Dynamical Cell Assembly Hypothesis - Theoretical Possibility of Spatio-temporal Coding in the Cortex. *Neural Netw* **9**, 1303-1350 (1996).
43 Carroll, M. S. & Ramirez, J. M. Cycle-by-cycle assembly of respiratory network activity is dynamic and stochastic. *Journal of neurophysiology* **109**, 296-305, doi:10.1152/jn.00830.2011 (2013).
44 Wang, X. *et al.* Laser ablation of Dbx1 neurons in the pre-Botzinger complex stops inspiratory rhythm and impairs output in neonatal mice. *Elife* **3**, e03427, doi:10.7554/eLife.03427 (2014).
45 Van Vreeswijk, C., Abbott, L. F. & Ermentrout, G. B. When inhibition not excitation synchronizes neural firing. *J Comput Neurosci* **1**, 313-321 (1994).
46 Bartos, M., Vida, I. & Jonas, P. Synaptic mechanisms of synchronized gamma oscillations in inhibitory interneuron networks. *Nat Rev Neurosci* **8**, 45-56, doi:10.1038/nrn2044 (2007).
47 Isaacson, J. S. & Scanziani, M. How inhibition shapes cortical activity. *Neuron* **72**, 231-243, doi:10.1016/j.neuron.2011.09.027 (2011).
48 Bernander, O., Koch, C. & Usher, M. The Effect of Synchronized Inputs at the Single Neuron Level. *Neural Computation* **6**, 622-641, doi:DOI 10.1162/neco.1994.6.4.622 (1994).
49 Shao, X. M. & Feldman, J. L. Respiratory rhythm generation and synaptic inhibition of expiratory neurons in pre-Botzinger complex: differential roles of glycinergic and GABAergic neural transmission. *Journal of neurophysiology* **77**, 1853-1860, doi:10.1152/jn.1997.77.4.1853 (1997).

50 Srivastava, K. H. *et al.* Motor control by precisely timed spike patterns. *Proc Natl Acad Sci U S A* **114**, 1171-1176, doi:10.1073/pnas.1611734114 (2017).
51 Mitchell, R. A. & Herbert, D. A. Synchronized high frequency synaptic potentials in medullary respiratory neurons. *Brain Res* **75**, 350-355 (1974).
52 Feldman, J. L., Sommer, D. & Cohen, M. I. Short time scale correlations between discharges of medullary respiratory neurons. *Journal of neurophysiology* **43**, 1284-1295, doi:10.1152/jn.1980.43.5.1284 (1980).
53 Ellenberger, H. H., Feldman, J. L. & Goshgarian, H. G. Ventral respiratory group projections to phrenic motoneurons: electron microscopic evidence for monosynaptic connections. *J Comp Neurol* **302**, 707-714, doi:10.1002/cne.903020403 (1990).
54 Huang, W. X., Cohen, M. I., Yu, Q., See, W. R. & He, Q. High-frequency oscillations in membrane potentials of medullary inspiratory and expiratory neurons (including laryngeal motoneurons). *Journal of neurophysiology* **76**, 1405-1412, doi:10.1152/jn.1996.76.3.1405 (1996).
55 Schmid, K., Bohmer, G. & Weichel, T. Concurrent fast and slow synchronized efferent phrenic activities in time and frequency domain. *Brain Res* **528**, 1-11 (1990).
56 Moore, J. D. *et al.* Hierarchy of orofacial rhythms revealed through whisking and breathing. *Nature* **497**, 205-210, doi:10.1038/nature12076 (2013).
57 Yackle, K. *et al.* Breathing control center neurons that promote arousal in mice. *Science* **355**, 1411-1415, doi:10.1126/science.aai7984 (2017).
58 Liu, G., Feldman, J. L. & Smith, J. C. Excitatory amino acid-mediated transmission of inspiratory drive to phrenic motoneurons. *Journal of neurophysiology* **64**, 423-436, doi:10.1152/jn.1990.64.2.423 (1990).
59 Ruangkittisakul, A., Kottick, A., Picardo, M. C., Ballanyi, K. & Del Negro, C. A. Identification of the pre-Botzinger complex inspiratory center in calibrated "sandwich" slices from newborn mice with fluorescent Dbx1 interneurons. *Physiol Rep* **2**, doi:10.14814/phy2.12111 (2014).
60 Migliore, M., Hoffman, D. A., Magee, J. C. & Johnston, D. Role of an A-type K+ conductance in the back-propagation of action potentials in the dendrites of hippocampal pyramidal neurons. *J Comput Neurosci* **7**, 5-15 (1999).
61 Dingledine, R., Borges, K., Bowie, D. & Traynelis, S. F. The glutamate receptor ion channels. *Pharmacol Rev* **51**, 7-61 (1999).
62 Narayanan, R. & Johnston, D. The h current is a candidate mechanism for regulating the sliding modification threshold in a BCM-like synaptic learning rule. *Journal of neurophysiology* **104**, 1020-1033, doi:jn.01129.2009 [pii] 10.1152/jn.01129.2009 (2010).
63 Hines, M. L. & Carnevale, N. T. The NEURON simulation environment. *Neural Comput* **9**, 1179-1209 (1997).
64 Torrence, C. & Compo, G. P. A practical guide to wavelet analysis. *B Am Meteorol Soc* **79**, 61-78, doi:Doi 10.1175/1520-0477(1998)079<0061:Apgtwa>2.0.Co;2 (1998).
65 Graupner, M. & Reyes, A. D. Synaptic input correlations leading to membrane potential decorrelation of spontaneous activity in cortex. *J Neurosci* **33**, 15075-15085, doi:10.1523/JNEUROSCI.0347-13.2013 (2013).

Acknowledgements

This work was supported by NIH-NHLBI grant 1R35HLI35779. We thank D.V.Buonomano, A.Kumar and R. Narayanan for their insights and discussion on this project and R. Abreu, D.N.Chiu, Hailan Hu, K.Kam, M.Shao and C.F.Yang for their comments on earlier versions of this manuscript.

Contributions

S.A and J.L.F designed and interpreted experiments, S.A performed experiments and analyzed data. S.A. and J.L.F critically evaluated data, wrote paper and approved the final version of the manuscript.